Eur Biophys J (2002) 31: 163–171
DOI 10.1007/s00249-001-0203-1

ARTICLE

Ehab I. Mohamed · Antonino de Lorenzo

Modeling combined transport of water and test macromolecules across the glomerular capillary barrier: dynamics of the permselectivity

Received: 8 August 2001 / Revised: 5 November 2001 / Accepted: 29 November 2001 / Published online: 25 January 2002

Abstract The structure, function, and composition of the basement membrane of the glomerular capillaries of the mammalian kidney have been extensively studied, in light of the membrane's important physiological role in glomerular filtration of macromolecules and of its frequent involvement in renal diseases. An analytical mathematical model, based on the fiber matrix theory, was developed to describe the dynamics of the permselective function of the glomerular capillary barrier using mainly its hemodynamic and morphometric variables. The glomerular basement membrane was represented as a homogeneous three-dimensional meshwork of fibers of uniform length (L_f), radius (R_f), and packing density (N_{fv}) and characterized by a local Darcy permeability (a measure of the intrinsic hydraulic conductance of the glomerular basement membrane). The model was appropriate for simulating in vivo fractional clearance data of neutral test macromolecules from an experimental rat model. We believe that the L_f and R_f best-fit numerical values, characterizing a glomerular basement membrane geometrical arrangement, may represent diagnostic measures for renal function in health and disease. That is, these parameters may signify new insights for the diagnosis of some human nephropathies and possibly may explain the beneficial effects and/or sites of action of some pharmacological modifiers (e.g., angiotensin converting enzyme inhibitors).

Keywords Fiber matrix theory · Hydraulic permeability · Darcy permeability · Fractional clearance · Mathematical modeling

E.I. Mohamed (✉) · A. de Lorenzo
Human Physiology Division,
Department of Neurosciences,
Faculty of Medicine and Surgery,
University of Rome "Tor Vergata",
Via Montpellier 1, 00133 Rome, Italy
E-mail: eimohamed@yahoo.com
Tel.: +20-3-4215455/2373/2331

A. de Lorenzo (✉)
Scientific Institute "S. Lucia", Rome, Italy
E-mail: delorenzo@uniroma2.it
Tel.: +39-06-72596415

E.I. Mohamed
Department of Biophysics, Medical Research Institute,
University of Alexandria, El Horreya Avenue 165,
21561 Alexandria, Egypt

Introduction

The complexity of the function and structure of the human kidney has inspired many researchers to analyze the nature of the alterations produced by renal pathologies in the intrinsic structure of the kidney (Farquhar and Palade 1961; Brenner et al. 1978; Mayers and Guasch 1993; Kalluri et al. 1997). With specific regard to the renal glomerulus, studies have shown that its function is to filter blood, producing a protein-free filtrate of the plasma while retaining the cellular elements of the blood and plasma proteins in the circulation (Tisher and Madsen 1991). Clearance studies carried out by physiologists since the 1950s using various probe molecules established that the glomerular capillary wall (GCW), as a whole, has both size-selective and charge-selective properties (Brenner et al. 1978), meaning that the passage of macromolecules across the GCW is increasingly restricted as their size and net negative charge increase (Farquhar 1975, 1991). To determine the mechanisms involved in the selectivity of the capillary wall of various human organs, many investigators have evoked the fiber matrix theory (i.e., the hypothesis that a random network of fibers located in or between the endothelial cells is the principal determinant of selectivity) (Michel 1978; Curry and Michel 1980; Fisher 1982; Curry 1984; Robinson and Walton 1989; Adamson 1992; Katz 1992). The concepts behind this theory were first introduced by Ogston, who developed mathematical formulas for the exclusion and diffusion of molecules in a uniform random suspension of fibers (Ogston 1958; Ogston et al. 1973). In the present study, we developed a mathematical model, based on the fiber matrix theory, to describe

the dynamics of combined transport of water and macromolecules across the GCW. The permselective function of the GCW was shorthanded mathematically to fit the experimental results of the fractional clearance of neutral graded-size macromolecules in healthy Munich-Wistar (MW) and control Munich-Wistar Frömter (MWF) rats subjected to micropuncture and morphometrical analysis.

Methods

Glomerular basement membrane biochemical and geometrical aspects

A three-dimensional (3D) network of irregular, poorly outlined strands observed at high magnification has been found to be the characteristic structure of basement membranes (Inoue and Leblond 1988). The strands consist of ubiquitous aggregates of at least five substances: a type IV collagen arranged as an axial fiber, three glycoproteins (laminin, nidogen, and fibronectin), and a proteoglycan (heparan sulfate) (Laurie et al. 1982; Sanes 1982; Timpl and Martin 1982; Laurie et al. 1984; Grant et al. 1985; Grant 1987). The model's unit element was defined as a type IV collagen tetramer (four collagen molecules connected at their 7S domain) (Mohamed 1994). This unit element forms a scaffold onto which other protein molecules can be incorporated to form an ideal basement membrane. We postulate that the arms of the collagen tetramer are distributed symmetrically in space (Fig. 1A). Laminin-1 molecules, with the aid of nidogen molecules, are attached to the collagen unit element, with their arms extending along the arms of this unit element, passing though the interfibril spaces. Double tracks of heparan sulfate proteoglycan wind their way up to the surface of the collagen unit element (Fig. 1B). Based on the unit element of Fig. 1B, we simulated (MiniCAD 6, Vectorworks, Nemetschek, USA) an ideal unit element consisting of four joined cylinders of uniform length (L_f) and radius (R_f) and arranged symmetrically in space (Fig. 1C). Figure 2 is a top view of a 3D section of an ideal glomerular basement membrane (GBM) produced by the simple repetition of the unit element of Fig. 1B along Cartesian coordinates (x, y, and z). The diffusion of solute molecules in the matrix depends on their radius and on the fiber's dimensions and density, which define the restrictive characteristics of the meshwork.

Assumptions and definitions

The GBM is considered to be a continuous homogenous membrane, which is entirely available for filtration and which consists of a 3D meshwork of symmetrical fibrous unit elements (Fig. 1B). Each arm of the fibrous unit element is considered to have the same L_f and R_f (Fig. 1C). The meshwork is uniform in density; thus the number of fibers per unit volume (N_{fv}) is constant throughout the meshwork. Since the system of fibrous unit elements is isotropic, for any element of volume, fiber orientation is defined by the angle between the fiber and a given line. In accordance with the definition of Ogston (1958), the size of spaces is defined by randomly choosing a point of origin in the meshwork and expanding a spherical surface from this point until it makes tangential contact with the nearest point between the joint ends of the arm of a fibrous unit element.

Mathematical formulation

The symmetrical nature of the fibrous unit element provides a simple geometrical means to determine fiber density (N_{fv}) in the fibrous meshwork. At any arbitrary point in the meshwork, a fibrous unit element is contained in an imaginary right hexagonal prism (Fig. 3) and N_{fv} is given by:

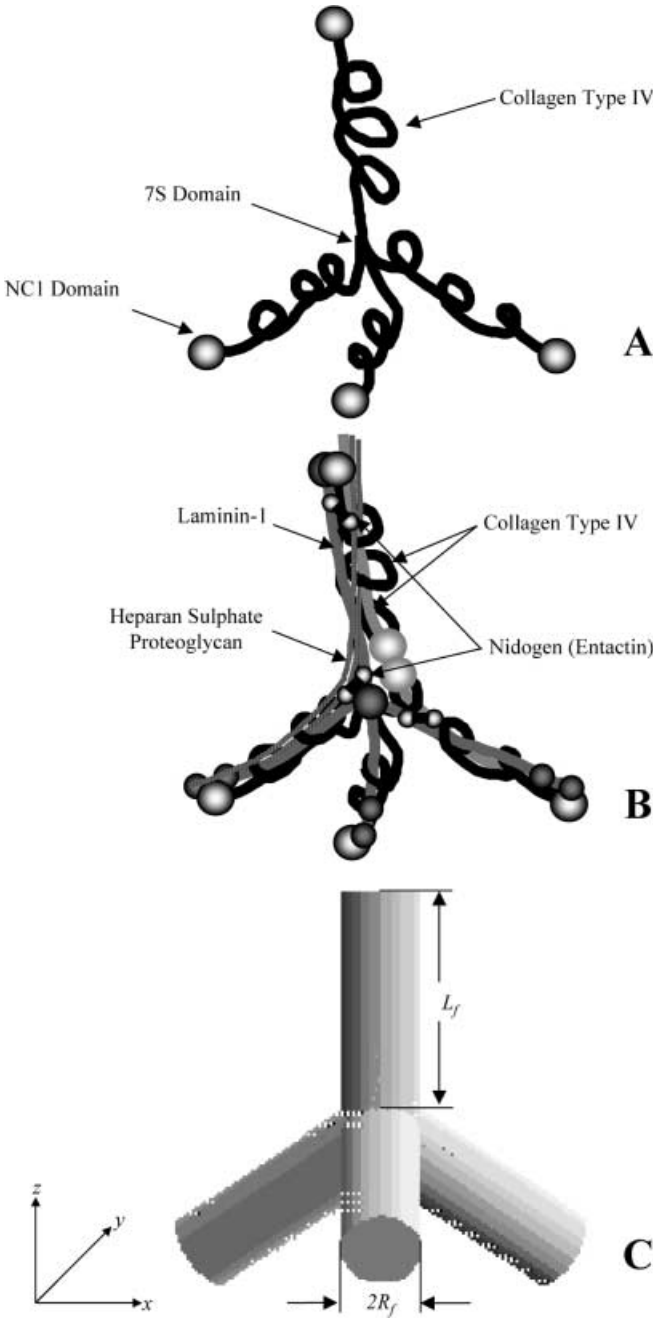

Fig. 1 **A** Schematic presentation of the fiber matrix unit element (type IV collagen tetramer) distributed symmetrically in space. **B** Other glomerular basement membrane proteins (laminin-1, heparan sulfate proteoglycan, and nidogen) connected to the collagen type IV unit element. **C** Computer simulation, using a commercially available software package, of an ideal unit element of characteristic length L_f and radius R_f, based on the unit element in **B**

$$N_{\mathrm{fv}} = 8 \Big/ \left[3\sqrt{3}L_{\mathrm{f}}^{3}(\cos 19.5)^{2}(1+\sin 19.5)\right] \left(\mathrm{cm}^{-3}\right) \quad (1)$$

For the sake of geometric simplicity, in making the calculations below, the ideal GBM was based on the ideal unit element in Fig. 1C. The total fractional solid volume (V_f) of the matrix of cylindrical fibers is given by:

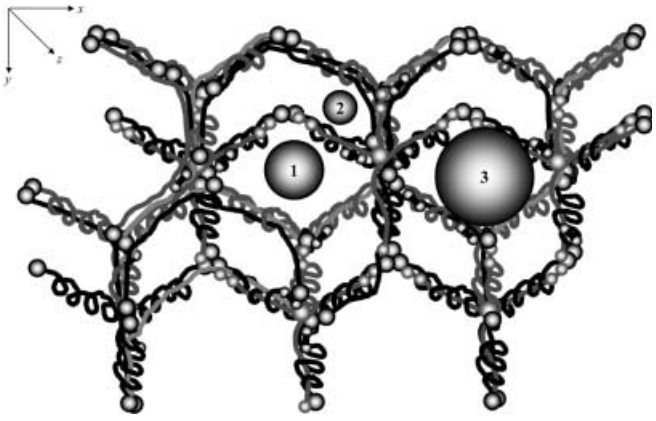

Fig. 2 Top view of a three-dimensional section of an ideal fiber matrix glomerular basement membrane together with permeating molecules of varying radius (labeled as *1*, *2*, and *3*)

$$V_f = \pi R_f^2 N_{fv} L_f - CF \tag{2}$$

where $CF = 2/3\pi N_{fv} R_f^3$ is a correction factor for the joined ends of the cylinders.

On the basis of the aforementioned assumptions (see above), we will derive a form for the probability distribution of spaces of size R_f in the 3D isotropic meshwork of joined fibrous unit elements shown in Fig. 2. The number of fibers with orientation angle Ψ laying at a tangential distance between R_f and $R_f + dR_f$ from a point of origin in the meshwork is given by:

$$(dN_t)_{R_f,\Psi} = 4\pi N_{fv} R_f^2 \, dR_f \, d\Psi / \sin^2\Psi \tag{3}$$

To obtain the total number of fibers at a tangential distance between R_f and $R_f + dR_f$ from the origin, we integrate the last equation in the interval between $\cot^{-1} L_f/2R_f$ and $\pi/2$ and express the total number of tangential contacts in terms of the unit increase in surface area of the sphere as it expands within the meshwork of fibers, which is given by:

$$dN_t/dS = N_{fv} L_f/4 \tag{4}$$

The size of spaces within the fibrous meshwork is defined by taking an arbitrary origin in the meshwork and expanding a spherical space around it until it reaches the nearest fiber. The probability (δP) that the spherical space lies between R_f and $R_f + dR_f$ is the combined probability that no tangential contact occurs within R_f of the origin ($1 - dN_t$) and at least one tangential contact (dN_t) occurs between R_f and $R_f + dR_f$ is given by the binomial distribution:

$$\delta P = n!/(n-1)!(dN_t/dS\delta S)(1 - dN_t/dS\delta S)^{n-1} \tag{5}$$

which is based on the assumption that changes in surface area as R_f expands from the point of origin to R_f are divided into equal increments (δS). In the limit of very large numbers of n, the binomial distribution (Eq. 5) reduces to a Poisson distribution, which represents the probability distribution of spaces of size R_f in a 3D meshwork of joined fibrous unit elements on the basis of neglecting the contribution of end-on contacts, since all unit element arm ends are connected to each other, given by:

$$dP/dR_f = 2\pi R_f N_{fv} L_f \exp\left(-\pi R_f^2 N_{fv} L_f\right) \tag{6}$$

This formula is the same as the formula derived on the basis of neglecting the contribution of end-on contacts because the fiber length was supposed to be much larger than fiber radius (i.e., $L_f \gg R_f$) (Ogston 1958; Curry 1984).

The extent to which a solute of radius a penetrates the meshwork is determined by the probability distribution of spaces with effective radii greater than $a + R_f$. The integration of Eq. (6) gives

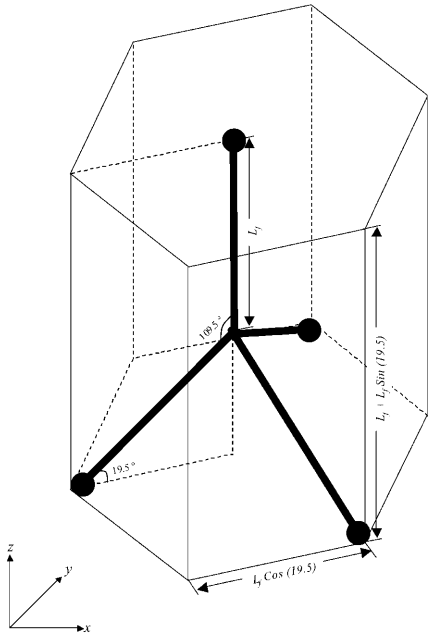

Fig. 3 The fiber matrix unit element of arm length L_f is contained in an imaginary right hexagonal prism of a side length $L_f \cos(19.5)$ and height $L_f + L_f \sin(19.5)$

the fraction of network volume (K_{af}) that will accommodate a solute of radius a, given by:

$$K_{af} = \exp\left[-\pi(a + R_f)^2 N_{fv} L_f\right] \tag{7}$$

On basis of Eq. (7), the partition coefficient (Φ_f), defined as the space available to a solute of radius a relative to the space available only to water (i.e., $a = 0$) (Ogston et al. 1973; Curry 1984), can be given by:

$$\Phi_f = \exp\left[V_f - V_f(1 + a/R_f)^2\right] \tag{8}$$

The molecular diffusion is described as the mechanism whereby low-molecular-weight hydrophilic and lipophilic solutes cross the GCW. For larger molecules, both diffusion and solvent drag determine the transcapillary flux (Ogston et al. 1973; Curry 1984). On the basis of Eq. (7), the diffusion coefficient (D_f) is thus given by:

$$D_f = D_0 \exp\left[-V_f^{1/2}(1 + a/R_f)\right] \left(\text{cm}^2\ \text{s}^{-1}\right) \tag{9}$$

where D_0 is the free diffusion coefficient for an ideal solution of Stokes-Einstein spheres at 37 °C. It has a magnitude of $3.24 \times 10^{-5}/a$ ($\text{cm}^2\ \text{s}^{-1}$) if a is measured in angstroms (Å). Equations (8) and (9) are then used to calculate the solute permeability coefficient (k_{sf}) of a membrane consisting of fibrous molecules (Curry 1984), which is given by:

$$k_{sf} = A_{net} \Phi_f D_f / S\Delta x \left(\text{cm}\ \text{s}^{-1}\right) \tag{10}$$

where A_{net} is the membrane area available for filtration, S is the total membrane surface area, and Δx is the membrane thickness.

The volume flux (J_v) is approximated by a function which is qualitatively correct and which satisfies the overall conservation of volume and test solutes for an entire capillary or glomerulus (Deen et al. 1985), given by:

$$J_v(y) = J_{va} \times e^{-by} (\text{cm}\ \text{s}^{-1}) \tag{11}$$

where J_{va} is the volume flux at the afferent end of the capillary and b is a constant. At the afferent end of the capillary, $J_{va} = k_h(\Delta P - \Pi_a)$, since $\Pi_a = \Pi_g$, where k_h is the GCW hydraulic permeability, ΔP is

the difference in the transmembrane hydraulic pressure, and Π_a is the colloid osmotic pressure at that point.

The membrane hydraulic permeability (k_h) is given by one of three formulas. The first is referred to as the hydrodynamic drag model (Curry 1984). It describes the drag forces exerted by fibers, which determine the pressure drop from parallel and perpendicular flow through randomly distributed fibers. k_h and the relative Darcy permeability (k_d) are given by:

$$k_h = 3R_f^2 A_{net}(1 - V_f)/4\eta S\Delta x V_f \left(\text{cm s}^{-1}\ \text{mmHg}^{-1}\right) \tag{12a}$$

$$k_d = 3R_f^2(1 - V_f)/4V_f\left(\text{cm}^2\right) \tag{12b}$$

where η is the glomerular filtrate viscosity, taken to be that of water at 37 °C (0.007 g cm^{-1} s^{-1}).

The second model is referred to as the hydraulic radius model (Curry et al. 1983). The hydraulic radius is defined as the volume available for water flow within the fibrous material divided by the surface area in contact with water. It describes water flow through a fibrous network within the principal water pathway of the capillary wall. k_h and relative k_d are given by:

$$k_h = A_{net}R_f^2(1 - V_f)^3 \Big/ 4G\eta S\Delta x V_f^2\left(\text{cm s}^{-1}\ \text{mmHg}^{-1}\right) \tag{13a}$$

$$k_d = R_f^2(1 - V_f)^3 \Big/ 4GV_f^2\left(\text{cm}^2\right) \tag{13b}$$

where G is the dimensionless Kozeny-Carman constant.

The third model we refer to as the numerical analysis model (Palassini and Remuzzi 1998). It describes water flow through viscous media. k_h and relative k_d are given by:

$$k_h = uR_f^2 A_{net}(-\ln V_f)^v/\eta S\Delta x (V_f)^w\left(\text{cm s}^{-1}\ \text{mmHg}^{-1}\right) \tag{14a}$$

$$k_d = uR_f^2(-\ln V_f)^v/(V_f)^w\left(\text{cm}^2\right) \tag{14b}$$

where u, v, and w are constant numerical values estimated by non-linear least-square fitting of numerical simulations of the viscous flow.

The dimensionless Péclet number (Pe) is defined as the ratio of the convection to diffusion velocities of a solute (Curry 1984). In a fibrous meshwork, Pe is given by:

$$Pe = J_v(y)(1 - \sigma_f)/k_{sf} \tag{15}$$

where k_{sf} is the solute permeability coefficient (given by Eq. 10), $J_v(y)$ is the volume flux (given by Eq. 11), and σ_f is the solvent-drag reflection coefficient. Assuming the hydraulic radius model, the flow between fibers can be described in a first approximation as ''pseudo-Poiseuillean'', and the relative form of σ_f in a fibrous network is thus given by:

$$\sigma_f = (1 - \Phi_f)^2 \tag{16}$$

The solute flux, $J_s(y)$, in terms of the concentration of solutes on the inner and outer sides of the GCW [$C_1(y)$ and C_2, respectively] and the volume flux [$J_v(y)$] (Curry 1984) is given by:

$$J_s(y) = J_v(y)(1 - \sigma_f)\left[C_1(y)e^{Pe} - C_2\right]/\left(e^{Pe} - 1\right)\left(\text{mol s}^{-1}\ \text{cm}^{-2}\right) \tag{17}$$

In the steady-state ultrafiltration, a simple mass balance on the solute on the (outer) low-pressure side of the homogeneous membrane requires the solute concentration on the outer side to be constant [i.e., $C_2 = J_s(y)/J_v(y)$] (Curry 1984). The concentration of solutes along the inner side of the GCW, $C_1(y)$, can be approximated by a function (Deen et al. 1985) given by:

$$C_1(y) = C_{1a}\left[1 + c_i\left(1 - e^{-by}\right)\right](\text{mol}) \tag{18}$$

The constant c_i is given by:

$$c_i = FF(1 - \theta_i)/(1 - FF)\left(1 - e^{-b}\right) \tag{19}$$

where FF is the filtration fraction of water and θ_i is an initial guess of the solute fractional clearance. Since the rate at which $C_1(y)$ increases is closely related to the volume flux, then on substituting C_2, $C_1(y)$, and $J_v(y)$, Eq. (17) becomes:

$$J_s(y) = C_{1a}J_{va}(1 - \sigma_f)\left[1 + a_i\left(1 - e^{-by}\right)\right]e^{Pe-by}/\left(e^{Pe} - \sigma_f\right)\left(\text{mol s}^{-1}\,\text{cm}^{-2}\right) \tag{20}$$

The solute fractional clearance, defined as the ratio of the solute's concentration in the filtrate to that in the plasma (Deen et al. 1985), is given by:

$$\theta = 1/C_{1a}\int_0^1 J_s(y)\mathrm{d}y \Big/ \int_0^1 J_v(y)\mathrm{d}y \tag{21}$$

Substituting $J_v(y)$ and $J_s(y)$ (Eq. 11 and Eq. 20, respectively), Eq. (21) becomes:

$$\theta = \alpha\int_0^1 \left[1 + \beta\left(1 - e^{-by}\right)\right]e^{Pe-by}/(e^{Pe} - \sigma_f)\mathrm{d}y \Big/ 1 + \alpha\beta\int_0^1 \left(1 - e^{-by}\right)e^{Pe-by}/(e^{Pe} - \sigma_f)\mathrm{d}y \tag{22}$$

where $\alpha = b(1 - \sigma_f)/\left(1 - e^{-b}\right)$ and $\beta = FF/(1 - FF)\left(1 - e^{-b}\right)$. Equation (22) is an analytical mathematical description of the fractional clearance of any test macromolecule. Based on this formula, we fitted the experimental fractional clearance of neutral test macromolecules, measured in the experimental rat model.

Method of solution

The numerical integrations of the continuous real-valued function $\theta = \theta(L_f, R_f, a)$ (given by Eq. 22), where L_f and $R_f \in R^n$ and $a \in R$, were calculated using the Simpson's composite quadratures (Johnson and Riess 1982). We fitted the experimental fractional clearance data [θ_i(expt)] of test macromolecules of varying size ($a = 2.6$–6.4 nm) for the MWF and MW rat strains by finding the optimal values of L_f and R_f that minimized the weighed sum of the squared errors, given by:

$$\chi^2 = \sum_{i=1}^{n}\left[(\theta_i(\text{expt}) - \theta_i(L_f, R_f, a_i))/\sigma_i\right]^2 \tag{23}$$

where n is the number of data points in the fractional clearance curve and σ_i is the standard error of θ_i(expt). We developed a non-linear least-square fitting program (Landriani et al. 1983) in Visual Basic 6 code (Edulearn, Md., USA) running on a Pentium 4 PC to find the best-fit L_f and R_f values.

The model's analytical equations were implemented into the non-linear least-square program, as shown by the simplified flowchart of Fig. 4. The glomerular hemodynamic variables (columns A and C, Table 1) were used to calculate the ultrafiltration coefficient (k_f) (step I), as described elsewhere (Deen et al. 1972). The glomerular ultrastructural morphometric variables (columns B and D, Table 1), in addition to the k_f resulting from step I, were used to calculate the overall hydraulic permeability (k_{tot}) of the GCW [and the relative contribution of its layers (endothelium, GBM, and epithelium) to the total water flow resistance] and the local Darcy permeability (k_d) (step II) (Drumond and Deen 1994). Once an initial guess of L_f is provided by the non-linear least-square fitting program, R_f is calculated using a bisection algorithm, which compares the k_d of step II and theoretical k_d calculated on the basis of any of Eqs. (12b), (13b), and (14b) (step III). The theoretical fractional clearance [$\theta_i(L_f, R_f, a)$] is calculated using numerical integrations of Eq. (22) (step IV). The numerical solution $\theta_i(L_f, R_f, a)$ of step IV is compared with the relative experimental observation at a given solute radius [θ_i(expt)], minimizing the weighed sum of the squared errors (χ^2) given by Eq. (23) (step V). On basis of the convergence of the lowest χ^2 value, the program terminates in giving an output file containing experimental and predicted fractional clearances and the model optimal output parameters L_f, R_f, V_f, and χ^2, together with descriptive statistical measures.

Results and discussion

Parameter values

The representative hemodynamic and morphometric input variables for MW rats (Oliver et al. 1992; Drumond and Deen 1994) and control MWF rats (Remuzzi et al. 1990; Iordache et al. 1994) are summarized in Table 1. The ultrafiltration coefficients and microhydrodynamic variables for both rat strains, as calculated using the glomerular ultrafiltration model (Deen et al. 1972) and the structural determinants model (Drumond and Deen 1994), respectively, are summarized in Table 2. The hydraulic permeability for the total GCW (k_{tot}) and for the individual epithelial and GBM layers (k_{ep} and k_{bm}, respectively) was lower for the MWF rats compared with the MW rats, as a result of differences in morphometric measurements between rat strains. The estimated local GBM Darcy permeability (k_d) was also lower for MWF rats compared with MW rats. Given that the local Darcy permeability provides an approximate indication of the porosity of

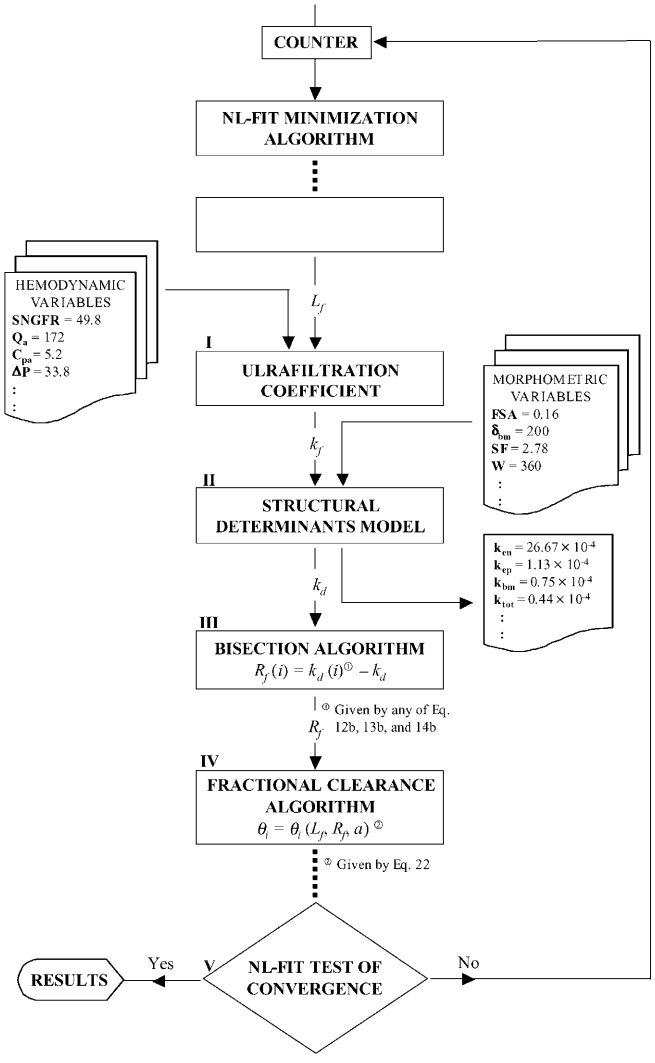

Fig. 4 A simplified flowchart of the non-linear least-square fitting program. *Step I*: hemodynamic input variables are fed to calculate the ultrafiltration coefficient (k_f). *Step II*: morphometric variables and k_f are fed to calculate the glomerular basement membrane local Darcy permeability (k_d) and individual layer hydraulic permeability contribution. *Step III*: applying a bisection algorithm, the program calculates the fiber radius R_f. *Step IV*: the program calculates the fractional clearance by numerically integrating Eq. (22). *Step V*: the program tests the convergence of the numerical solution of the lowest weighed sum of squared errors given by Eq. (23)

Table 1 Hemodynamic and morphometric input variables measured for normal euvolumic Munich-Wistar (MW) and control Munich-Wistar Frömter (MWF) rats

	MW	MWF
Hemodynamic variables	A[a]	B[b]
Single-nephron glomerular filtration rate, SNGFR (nL min^{-1})	49.8	47
Afferent plasma flow rate, Q_a (nL min^{-1})	172	161
Afferent plasma protein concentration, C_{pa} (g dL^{-1})	5.2	5.3
Mean glomerular transcapillary pressure, ΔP (mmHg)	33.8	38
Morphometric variables	C[c]	D[d]
Membrane filtering surface area, FSA (mm^2)	0.16	0.29
Glomerular basement membrane thickness, δ_{bm} (nm)	200	161
Filtration slit frequency, SF (μm^{-1})	2.78	1.45
Width of the structural unit, W (nm)	360	690
Filtration slit width, W_s (nm)	39	39
Number density of fenestrae, N_f/W (m^{-1})	8.33×10^6	8.33×10^6
Fractional area of fenestrae, ϵ_f	0.20	0.20
Fractional area of filtration slits, ϵ_s	0.11	0.06
Hydraulic permeability of endothelium, k_{en} (cm s^{-1} $mmHg^{-1}$)	2.67×10^{-3}	2.67×10^{-3}
Hydraulic permeability of epithelial slits, k_s (cm s^{-1} $mmHg^{-1}$)	1.05×10^{-3}	1.05×10^{-3}

[a]Oliver et al. (1992)
[b]Remuzzi et al. (1990)
[c]Drumond and Deen (1994)
[d]Iordache et al. (1994)

Table 2 Theoretical glomerular capillary wall ultrafiltration coefficients and hydrodynamic variables calculated for the Munich-Wistar (MW) and Munich-Wistar Frömter (MWF) experimental rat models

	MW	MWF
Ultrafiltration coefficients		
Glomerular ultrafiltration coefficient, k_f (nL min^{-1} $mmHg^{-1}$)	4.26	3.06
Hydrodynamic variables		
Hydraulic permeability of epithelium, k_{ep} (cm s^{-1} $mmHg^{-1}$)	1.13×10^{-4}	0.59×10^{-4}
Hydraulic permeability of GBM, k_{bm} (cm s^{-1} $mmHg^{-1}$)	0.75×10^{-4}	0.25×10^{-4}
Total GCW hydraulic permeability, k_{tot} (cm s^{-1} $mmHg^{-1}$)	0.44×10^{-4}	0.18×10^{-4}
Local membrane Darcy permeability, k_d (nm^2)	1.66	0.99

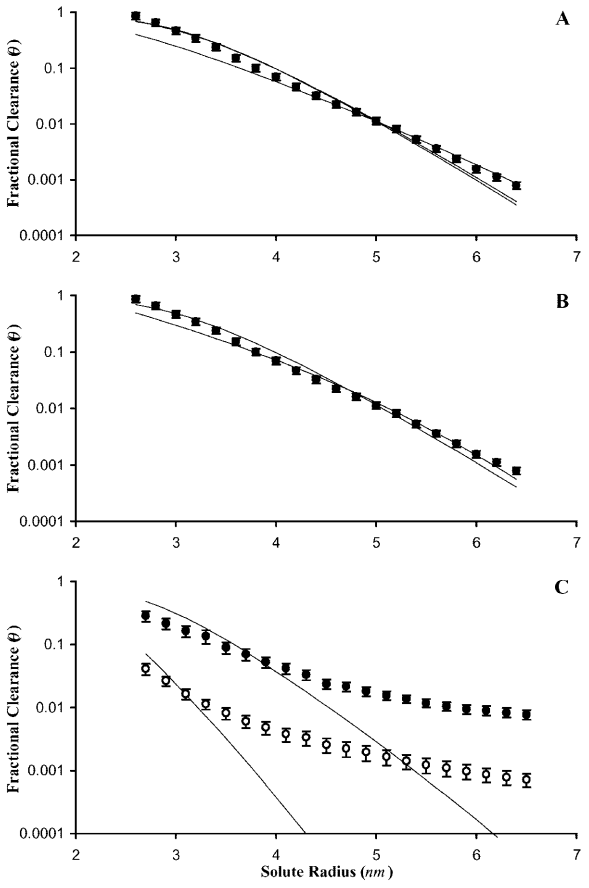

Fig. 5 **A** Different fiber matrix model curve fittings to experimental fractional clearance of dextrans (*solid circles*) measured for MWF rats (Remuzzi et al. 1990), shown as mean ± SD. The curve shape depends on the hydraulic permeability model implemented (*solid line*, hydraulic radius; *dashed line*, hydrodynamic drag; *dotted line*, numerical analysis). **B** Comparison between the fiber matrix model [θ(hydraulic radius), *solid line*] and the log-normal pore model (*dashed line*) fitting curves to experimental clearance of dextrans (*solid circles*) (Remuzzi et al. 1990). The fiber matrix model fits well with all solute ranges. **C** Fiber matrix model [θ(hydraulic radius)] fitting curves (*solid line*) for experimental fractional clearance of dextrans (*solid circles*) and ficolls (*open circles*) measured for the MW rats (Oliver et al. 1992). Experimental measurements are shown as mean ± SE

the basement membrane and of the radius of the constituent fibers, we deduce that the differences in k_d between the two rat strains might derive from differences in the spatial array, dimensions, and/or structure of the fibrous unit element.

Simulations of in vivo dextran clearance data from MWF rats

We chose the experimental dextran clearance data in the MWF rat strain to represent homoporous models, since this data set has been shown to be different from most other clearance studies in that there is no evidence for a second large pore or shunt when simulated using the conventional log-normal distribution pore model (Remuzzi et al. 1990). The non-linear least-square fitting curves of the fiber matrix model to the MWF rat strain clearance data are plotted in Fig. 5A. Different model forms, based on the hydraulic permeability formulas (Eqs. 12a, 13a, 14a) [θ(hydrodynamic drag), θ(hydraulic radius), and θ(numerical analysis)], fitted the clearance data well. The optimal fiber dimensions for each simulation are provided in Table 3, together with the χ^2 values as a measure of goodness of fit. The optimal L_f and R_f provided by θ(hydrodynamic drag) (5.06 nm and 2.00 nm, respectively) are consistent with measurements from electron microscopy studies (Leblond and Inoue 1989) (mean $L_f = 5.80$ nm, with $R_f = 1.50$–2.00 nm). The model θ(hydraulic radius) provided an optimal L_f of 4.67 nm and an R_f of 1.05 nm, which are also consistent with the values obtained with electron microscopy; the R_f is very similar to that of type IV collagen (~1 nm) (Timpl and Martin 1982). The estimates provided by θ(numerical analysis) are comparable to those of θ(hydraulic radius) (see Table 3). In addition, the total fractional solid volume of fibers (V_f) provided by θ (hydrodynamic drag) constitutes ~50% of the GBM volume, which far exceeds the 10–20% found by in vitro quantifications of GBM dry weight (Gekle et al. 1966; Daniels et al. 1992). However, the V_f for θ(hydraulic radius) and θ(numerical analysis) (18% and 14%, respectively) was within these limits. Although θ(hydraulic radius) and θ(numerical analysis) were not visually different (Fig. 5A), θ(hydraulic radius) had a lower χ^2 value (1.46) in comparison with θ(numerical analysis) (1.74) (Table 3). We thus deduce that the θ(hydraulic radius) fiber matrix model is the most suitable model for simulating dextran clearance data.

Table 3 Fiber matrix model output variables calculated on the basis of different hydraulic permeability models in comparison with pore model output variables. Optimal values were obtained by non-linear least-square fitting to experimental fractional clearance [θ_i(expt)] data from MWF rats

Fiber matrix model	L_f (nm)[a]	R_f (nm)	V_f	χ^2
Hydrodynamic drag model	5.06	2.00	0.47	1.44
Hydraulic radius model	4.67	1.05	0.18	1.46
Numerical analysis model	4.60	0.90	0.14	1.74
Pore model	μ	S		χ^2
Log-normal distribution	42.94	1.19		0.94

[a] L_f, fiber length; R_f, fiber radius; V_f, fractional fibers solid volume; χ^2, weighed sum of squared errors; μ, mean pore radius; S, standard deviation of pore distribution

For comparison purposes, we applied a log-normal distribution pore model ($\mu = 42.94$ and $S = 1.19$) to fit the same dextran clearance data (Remuzzi et al. 1990). Figure 5B demonstrates the capability of both the θ(hydraulic radius) model and the log-normal pore model to fit experimental clearance data. Although the pore model has a better χ^2 value (0.94) than the θ(hydraulic radius) model (1.46), the latter provides a more realistic morphological description of the GBM (see Table 3).

Simulations of in vivo dextran and ficoll clearance data from MW rats

Moreover, we applied the θ(hydraulic radius) model to mathematically simulate other clearance data of experimental test macromolecules (dextrans and ficolls) in the MW rat strain (Oliver et al. 1992). Figure 5C plots both experimental data points and their relative fitting curves, which did not adhere perfectly. This is consistent with similar observations for the same clearance data yet using a hydrodynamic model for hindered transport of macromolecules through a planar row of infinitely long cylinders spanning the glomerular slit diaphragms (Drumond and Deen 1995). A possible explanation of this finding is that these dextran and ficoll clearance data in the MW rat strain are bimodal, which has been previously shown to be poorly described by homoporous models (including the log-normal pore distribution model), requiring the presence of shunts (or large pores) (Oliver et al. 1992). This suggests that the present θ(hydraulic radius) model behaves as a homoporous model, since it simulated dextran clearance data in the MWF rat strain better than the two-pore dextran and ficoll clearance data in the MW rat strain.

Analysis of the fiber matrix model

Based on optimal fiber matrix output variables (Table 3), we analyzed the specific functions of the fiber matrix model (Eqs. 8, 9, and 15). The partition coefficient Φ_f describes the probability distribution of space available to a solute of radius a. The extent to which this solute penetrates a fiber meshwork (with a characteristic fiber radius R_f) is determined by the probability distribution of spaces with actual radii larger than $a + R_f$ (Ogston 1958; Curry 1984). Figure 6A plots the mathematical predictions of the exclusion power of a 3D meshwork of fibers at different V_f values. A fiber meshwork with a V_f of 0.47 has a greater exclusion power than a meshwork with a V_f of 0.18 or 0.14. The exclusion power increases with increasing permeating molecular radius a or specific fiber L_f and/or R_f (Eq. 8), which is verified by the Φ_f decrease along four orders of magnitude. Moreover, the fractional diffusion coefficient D_f/D_0 (Eq. 9) decreases linearly with increasing permeating molecular radius a at different V_f values (Fig. 6B). We can deduce that the radius of dextran molecules ($a = 2.6$–6.4 nm) (Remuzzi et al. 1990) varies from $1.3R_f$ to $3.2R_f$ in the θ(hydrodynamic drag) model. Although the radii greatly differ for the θ(hydraulic radius) and θ(numerical analysis) models (2.5–$6.1R_f$ and 2.9–$7.1R_f$, respectively) with respect to the radii in the θ(hydrodynamic drag) model, the difference had minor effects on the D_f/D_0 value, which decreases linearly, on average, from 0.21 to 0.05, with increasing permeating molecular radius. The exclusion power of the GBM in the present study is about three times greater than the theoretical exclusion power predicted by computer simulations for random fiber arrangements ($D_f/D_0 = 0.60$–0.10) (Booth and Lumsden

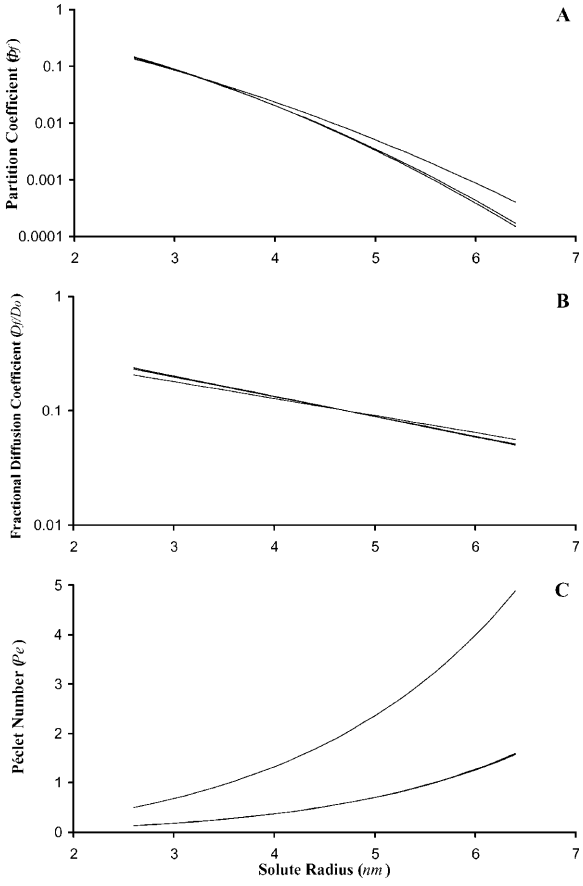

Fig. 6 **A** Mathematical predictions for exclusion in a 3D symmetrical meshwork of fibers, presented by the partition coefficient (Φ_f). As the solute radius increases, the fiber matrix restricts the passage of the solute. A fiber matrix with a fractional solid volume (V_f) of 0.47 (*solid line*) restricts solutes more effectively than a matrix with a V_f of 0.18 (*dashed line*) or 0.14 (*dotted line*). **B** Linear decrease in the fractional diffusion coefficient D_f/D_0 in a 3D symmetrical meshwork of fibers. Note the minimal differences among functional behaviors at the three fiber matrix densities. Note also the low diffusion of large solutes (radius range 4.8–6.4 nm) of the hydrodynamic drag (*solid line*) model. **C** Functional dependence of the Péclet number on permeating solute radius. For a highly dense matrix the hydrodynamic drag (*solid line*) *Pe* values range from 0.5 to 4.9 for a solute radius ranging from 2.6 to 6.4 nm. For less dense matrices, i.e. hydraulic radius (*dashed line*) and numerical analysis (*dotted line*), the *Pe* ranges from 0.1 to 1.6 for the same range of solute radius

1993). Finally, the dimensionless Péclet number (Eq. 15) is defined as the ratio of convection velocity to diffusion velocity of a permeating solute. The *Pe* increases proportionally with the solute radius (Fig. 6C). For a very dense matrix [θ(hydrodynamic drag)], *Pe* increases very rapidly with increasing radius, whereas for less dense matrices [θ(hydraulic radius) and θ(numerical analysis)], the *Pe* is comparatively low for the same range of radii and increases less rapidly.

Conclusions

A novel mathematical model, based on the fiber matrix theory, was developed analytically to interpret previously published experimental fractional clearance data of neutral test macromolecules in the MW and MWF rat strains. The fitting results showed the capability of the present model to describe the glomerular permselective function and to predict the effects of the hemodynamic and morphometric variables on GBM composition in the MWF rat strain. Thus the θ(hydraulic radius) model can predict the relative effect of alterations in the hemodynamic and morphometric variables, resulting from renal pathologies or pharmacological therapy, on the GBM fiber matrix composition given by L_f and R_f, which may represent diagnostic measures for renal function in humans. The results also suggest that the fiber matrix model is just as suitable for the simulation of fractional clearance data in vivo as conventional pore models with the same number of adjustable parameters, yet it is more realistic and may provide elastic geometrical solutions for the GBM in various functional states.

One of the model's basic assumptions is that the GBM represents the principal size and charge filtration barrier to circulating macromolecules, as reported by electron-dense tracer permeability studies using a variety of anionic and neutral tracers, which did not penetrate beyond the lamina rara interna of the GBM (Farquhar et al. 1999). This is consistent with the findings that the GBM constitutes ~60% and 70% of the total hydraulic resistance in the MW and MWF rat strains, respectively, as calculated using a structural determinants model for glomerular hydraulic permeability (Drumond and Deen 1994). Attention must be drawn to the GBM as the only complex and continuous barrier retaining essential blood cellular components and plasma proteins in the circulation. Additional investigations should concentrate on developing models for asymmetric fibrous unit elements in a heterogeneous meshwork and/or integrating epithelial slit pore models (Edwards et al. 1999) for simulating complex clearance data from proteinuric rats and nephritic humans.

Acknowledgements The professional editorial assistance of Mr. Mark Kanieff is very much appreciated.

References

Adamson RH (1992) An extension of the fiber matrix model of vascular permeability. Microvas Res 43:352–356

Booth JW, Lumsden CJ (1993) Explaining glomerular pores with fiber matrices. A visualization study based on computer modeling. Biophys J 64:1727–1734

Brenner BM, Hostetter TH, Humes HD (1978) Molecular basis of proteinuria of glomerular origin. N Engl J Med 298:826–833

Curry FE (1984) Mechanics and thermodynamics of transcapillary exchange. In: Renken EM, Michel CC (eds) Handbook of physiology, section 2, vol. IV, part 1: cardiovascular system. American Physiology Society, Bethesda, pp 309–374

Curry FE, Michel CC (1980) A fiber matrix model of capillary permeability. Microvas Res 20:96–99

Curry FE, Huxley VH, Adamson RH (1983) Permeability of single capillaries to intermediate sized colored solutes. Am J Physiol (Heart Circ Physiol 14) :H495–H505

Daniels BS, Hauser EB, Deen WM, Hostetter TH (1992) Glomerular basement membrane: in vitro studies of water and protein permeability. Am J Physiol (Renal Fluid Electrolyte Physiol 31) 262:F919–F926

Deen WM, Robertson CR, Brenner BM (1972) A model of glomerular ultrafiltration in the rat. Am J Physiol 223:1178–1183

Deen WM, Bridges CR, Brenner BM, Myers BD (1985) Heteroporous model of glomerular size selectivity: application to normal and nephrotic humans. Am J Physiol (Renal Fluid Electrolyte Physiol 18) 249:F374–F389

Drumond MC, Deen WM (1994) Structural determinants of glomerular hydraulic permeability. Am J Physiol 266:F1–F12

Drumond MC, Deen WM (1995) Hindered transport of macromolecules through a single row of cylinders: application to glomerular filtration. J Biomech Eng 117:414–422

Edwards A, Daniels BS, Deen WM (1999) Ultrastructural model for size selectivity in glomerular filtration. Am J Physiol (Renal Fluid Electrolyte Physiol 45) 276:F892–F902

Farquhar MG (1975) The primary glomerular filtration barrier – basement membrane or epithelial slits? Kidney Int 8:197–211

Farquhar MG (1991) The glomerular basement membrane: a selective macromolecular filter. In: Hay ED (ed) Cell biology of extracellular matrix. Plenum, New York, pp 365–418

Farquhar MG, Palade GE (1961) Glomerular permeability. II. Ferritin transfer across the glomerular capillary wall in nephritic rats. J Exp Med 114:699–716

Farquhar MG, Wissig SL, Palade GE (1999) Glomerular permeability. I. Ferritin transfer across the normal glomerular capillary wall. J Am Soc Nephrol 10:2645–2662

Fisher RF (1982) The water permeability of basement membrane under increasing pressure: evidence for a new theory of permeability. Proc R Soc London Ser B 216:475–496

Gekle D, Bruchhausen F von, Fuchs G (1966) Über die grösse der porenäquivalente in isolierten basalmembranen der rattennierenrinde. Arch Ges Physiol 289:180–190

Grant DS (1987) The application of immunogold histochemistry to the quantitative analysis of basement membrane. Thesis, McGill University

Grant DS, Kleinman HK, Leblond CP, Inoue S, Chung AE, Martin GR (1985) The basement-membrane-like matrix of the mouse EHS tumor. II. Immunohistochemical quantitation of six of its components. Am J Anat 174:387–398

Inoue S, Leblond CP (1988) Three-dimensional network of cords: the main component of basement membranes. Am J Anat 181:341–348

Iordache BE, Imberti O, Foglieni C, Remuzzi G, Bertani T, Remuzzi A (1994) Effects of angiotensin converting enzyme inhabition on glomerular capillary wall ultrastructure in MWF/Ztm rats. J Am Soc Nephrol 5:1378–1384

Johnson LW, Riess RD (1982) Numerical analysis. Addison-Wesley, New York

Kalluri R, Shield CF, Todd P, Hudson BG, Neilson EG (1997) Isoform switching of type IV collagen is developmentally arrested in X-linked Alport syndrom leading to increased susceptibility of renal basement membranes to endoproteolysis. J Clin Invest 99:2470–2478

Katz MA (1992) Structural change in fiber matrix allows for enhanced permeability and reduced hydraulic conductivity. Microvas Res 43:1–6

Landriani GS, Guardabasso V, Rocchetti M (1983) NL-FIT: a microcomputer program for non-linear fitting. Comp Prog Biomed 16:35–42

Laurie GW, Leblond CP, Martin GR (1982) Localization of type IV collagen, laminin, heparan sulfate proteoglycan, and fibronectin to the basal lamina of basement membranes. J Cell Biol 95:340–344

Laurie GW, Leblond CP, Inoue S, Martin GR, Chung A (1984) Fine structure of the glomerular basement membrane and immunolocalization of five basement membrane components to the lamina densa (basal lamina) and its extensions in both glomeruli and tubules of the rat kidney. Am J Anat 169:463–481

Leblond CP, Inoue S (1989) Structure, composition, and assembly of basement membranes. Am J Anat 185:367–390

Mayers BD, Guasch A (1993) Selectivity of the glomerular filtration barrier in healthy and nephrotic humans. Am J Nephrol 13:311–317

Michel CC (1978) The measurement of permeability in single capillaries. Arch Int Physiol Biochem 86:657–667

Mohamed EI (1994) Theoretical and morphological study of the glomerular size-selective function. Thesis, Alexandria University

Ogston AG (1958) The spaces in a uniform random suspension of fibers. Trans Faraday Soc 54:1745–1757

Ogston AG, Preston BN, Wells JD (1973) On the transport of compact particles through solutions of chain-polymers. Proc R Soc London Ser A 333:297–316

Oliver JD, Anderson S, Troy JL, Brenner BM, Deen WM (1992) Determination of glomerular size-selectivity in the normal rat with ficoll. J Am Soc Nephrol 3:214–228

Palassini M, Remuzzi A (1998) Numerical analysis of viscous flow through fibrous media: a model for glomerular basement membrane permeability. Am J Physiol (Renal Fluid Electrolyte Physiol 43) 274:F223–F231

Remuzzi A, Puntorieri S, Battaglia C, Bertani T, Remuzzi G (1990) Angiotensin converting enzyme inhibition ameliorates glomerular filtration of macromolecules and water and lessens glomerular injury. J Clin Invest 85:541–549

Robinson GB, Walton HA (1989) Glomerular basement membrane as a compressible ultrafilter. Microvas Res 38:36–48

Sanes JR (1982) Laminin, fibronectin, and collagen in synaptic and extrasynaptic portions of muscle fiber basement membrane. J Cell Biol 93:442–451

Timpl R, Martin GR (1982) Components of basement membranes. In: Furthmayr H (ed) Immunohistochemistry of the extracellular matrix. CRC Press, Boca Raton, pp 119–150

Tisher CC, Madsen KM (1991) Anatomy of the kidney. In: Brenner BM, Rector FC (eds) The kidney. Saunders, Philadelphia, pp 3–75